Advances and Applications in Electroceramics
Edited by K. M. Nair, Quanxi Jia and Shashank Priya

Magnetoelectric Multiferroics

Advances and Applications in Electroceramics
Edited by K. M. Nair, Quanxi Jia and Shashank Priya

FINITE-SIZE EFFECTS IN NANOSCALED MULTIFERROICS

J. J. Heremans (1), J. Zhong (2,3), R. Varghese (2,3), G. T. Yee (4), and S. Priya (2,3)
1) Department of Physics, Virginia Tech, Blacksburg, Virginia 24061, USA
2) Center for Energy Harvesting Materials and Systems, Virginia Tech, Blacksburg, Virginia 24061, USA
3) Department of Materials Science and Engineering & Department of Mechanical Engineering, Virginia Tech, Blacksburg, Virginia 24061, USA
4) Department of Chemistry, Virginia Tech, Blacksburg, Virginia 24061, USA

ABSTRACT

We present studies of single-phase multiferroic materials in nanoparticle or nanoplate form, where size effects modify the long range magnetic structure and hence influence the magnetic properties. Size effects as isolated here, are of particular relevance to understand the interplay between magnetic and ferroelectric properties in heterogeneous, multi-phase multiferroic structures. Bulk multiferroic $BiMnO_3$ shows ferromagnetic ordering below 105 K, but few characterization attempts have been performed on nanoscaled material. We have synthesized $BiMnO_3$ nanoplates and characterized the structure, composition, morphology and magnetic properties. Ferromagnetic behavior is not observed in the nanoplates, in contrast to the bulk, indicative of finite size effects. We have also synthesized $BiFeO_3$ nanoparticles (characterized by XRD, EDS and magnetometry), which exhibit ferromagnetism with spin-glass-like behavior, as a result of reduced dimensionality. Bulk perovskite $BiFeO_3$ instead shows antiferromagnetism. The difference in magnetic behavior for nanoparticles compared to bulk behavior, is, in both cases, attributable to finite-size effects.

INTRODUCTION

Magnetoelectric multiferroic single-phase materials are characterized by the presence of directly coupled ferroic orders, typically ferromagnetism and ferroelectricity. Attempts to identify single-phase systems exhibiting both ferromagnetic and ferroelectric orders hark to a study by Landau and Lifshitz analyzing the presence of magnetoelectric coupling on the basis of crystal symmetry, which led to theoretical and experimental work on Cr_2O_3 [1-4]. The magnetoelectric coupling in principle allows a technologically relevant control of magnetization by electric fields [5]. In particular, multiferroic materials offer potential applications in information storage, in spintronics and in sensors, where the magnetoelectric coupling can be used for multi-state functionalities [6]. However materials limitations exist on the types of single-phase structures in which the coupling can exist [7,8], and even then, in most single-phase materials the coupling is weak [9,10]. Several single-phase multiferroics have been reported in the literature, including $Ni_3B_7O_{13}I$, RMn_2O_5 (R: rare earths), $Ni_3V_2O_8$, $CoCr_2O_4$, $MnWO_4$, and $Pb(Fe_{2/3}W_{1/3})O_3$ [11-17], and the origin of the coupling between magnetic and ferroelectric degrees of freedom is under study. However, the search for high temperature single phase materials exhibiting a magnetoelectric effect of useful magnitude continues. Indeed in most single-phase

materials studied so-far, the orders and their coupling occur much below room temperature, since Néel or Curie temperatures are low [18]. Several avenues exist however to circumvent the present limitations on single-phase materials. Bilayers in which individual layers are coupled via strain have shown much promise, and, as another avenue, here we present examples how the ferroic orders of materials can be altered by reduced dimensions, with as specific examples $BiMnO_3$ (BMO) and $BiFeO_3$ (BFO). Size effects can introduce changes in physical behavior and offer the opportunity to tailor the physical properties. For example, BFO is known to exhibit antiferromagnetism in bulk form, yet several studies have suggested the onset of ferromagnetic behavior in BFO thin films and nanoparticles [19, 20].

BISMUTH MANGANESE OXIDE NANOPLATES

Among the multiferroic single-phase materials, BMO is a promising candidate for applications, but experiments on BMO have focused on bulk or thin film materials, with few attempts at nanoscale dimensions. Perovskite-phase BMO is typically synthesized under pressures of 40 - 50 kbar in the temperature (T) range of 600 - 900°C which results in stabilization of the desired perosvskite phase [21]. In this work, we have attempted synthesis of BMO nanoplates by the co-precipitation method. Stoichiometric quantities of Bi_2O_3 and $MnCl_2$ were dissolved in HNO_3 and HCl and NaOH was subsequently added to form the hydroxide gel. The gel was continuously stirred for 4 - 6 hours with T maintained at 100°C. The resulting crystalline powder was subsequently filtered and dried, and was found to consist of two phases, which were characterized by various methods. X-ray diffraction (XRD), energy dispersive X-ray spectroscopy (EDS), X-ray photoelectron spectroscopy (XPS), SEM and TEM were employed to characterize the structure, composition and morphology of the phases. SQUID magnetometry was applied for characterization of the ensemble magnetic properties.

Figures 1(a) and (b) depict TEM and SEM micrographs of as-synthesized material. Although nanoscale plates (area marked as "1" in Fig. 1(a), and dominant in Fig. 1(b)) form the majority of the material, a concentration of needle-shaped particles (area marked as "2" in Fig. 1(a)) was identified along with nanoplates in the TEM micrograph. The XRD pattern shown in Fig. 2 did not detect the presence of a secondary phase and indicates single-phase BMO. The major fraction of the material is hence BMO, corresponding with the dominant plate shape. Peak broadening is visible in the XRD due to the reduced dimensions of the BMO nanoplates. TEM-EDS analysis (Table I-top) on the needle-like phase, in the area marked as "2" in Fig. 1(a), shows that the needle-phase has substantially lower Mn content than Bi content. On the other hand, EDS analysis on the BMO nanoplates (Table I-bottom), conducted on the area marked as "1" in Fig. 1(a), shows Mn content to be slightly off-stoichiometry, and higher than Bi. Thus, the minority needle shape is a Bi-rich phase, while the majority BMO phase has a plate shape, and dominates the XRD pattern. The majority phase also likely dominates the magnetic properties.

The presence of multiferroicity in BMO was proposed by Hill and Rabe [22] and was experimentally confirmed by Sugawara *et al.* [23,24] and Kimura *et al.* [25]. Bulk BMO exhibits a ferromagnetic transition around $T = 105$ K [26]. Measurement of ferroelectric polarization on the

other hand has been hampered due to high electric leakage currents. We performed measurements of magnetization (M) at T = 10 K, 77 K and 298 K, as function of applied magnetic field (H). Magnetic hysteresis loops could not be identified from 298 K down to 10 K, precluding ferromagnetic behavior in the ensemble and hence also in the BMO nanoplates. Rather, paramagnetic behavior could be concluded in the sample, as shown in Fig. 3. Figure 3 depicts the T dependence of the susceptibility (χ, defined as $\chi = M(T)/H$) at fixed H under zero field cooling (ZFC) and field cooling (FC) conditions ($M(T)$ was measured under an applied H = 5000 Oe). The difference in $M(T)$ between ZFC and FC conditions never exceeds ~ 10 %, and hence irreversibility or spin-glass behavior are concluded to be absent. In short, no ferromagnetic transition was observed, indicating a loss of ferromagnetic order in these BMO nanoparticles.

In order to correlate the observed BMO slight non-stoichiometry to changes in valence state of the Mn ions, we performed a comparative XPS analysis. Figure 4 shows the XPS spectrum on four different materials: the BMO nanoplates, $MnCO_3$, Mn_2O_3 and MnO_2, with the latter three samples used as standard references corresponding to Mn valence states of +2, +3, and +4. If the XPS signal from the BMO sample coincides with one of the standards, the dominant Mn valence can be approximated. The results in Fig. 4 demonstrate that one peak position for the BMO nanoplates matches Mn_2O_3, indicating a Mn valence state in BMO of +3. However, XPS spectra of BMO samples also exhibit a signal in the binding energy range 650 eV - 645 eV. Hence other Mn valence states exist in the BMO nanoplates, as expected due to non-stoichiometry. This result also explains the presence of minor traces of needle shaped particles. The varying Mn valence can contribute to the deletion of the ferromagnetic transition, while another important contribution can be found in the nanoscale morphology.

BMO hosts three crystallographically distinct Mn^{3+} sites, and supports 6 different Mn-O-Mn superexchange pathways [26, 27]. The ferromagnetic order in bulk BMO originates in the Mn-O-Mn orbital configurations with ferromagnetic interactions outnumbering and dominating over the non-ferromagnetic configurations. A dominant collinear ferromagnetic ordering hence appears with an average Mn^{3+} magnetic moment of 3.2 μ_B [27], but the non-ferromagnetic interactions lead to partial frustration and a lower spin value than in the fully aligned case [26, 27]. Dynamic light scattering measurements in our samples show an average plate size of the BMO phase of ~120 nm in diameter. SEM and TEM micrographs (Fig. 1) imply a thickness much less than the diameter, hence the identification with a nanoplate morphology. In analogy to size effects mentioned for BFO, the low dimensionality of the BMO nanoplates can be invoked for the loss of ferromagnetism, resulting from alterations in the superexchange mechanism. We surmise that the low dimensionality of the nanoplates affects the length and the angle of Mn-O-Mn bonds, causing the delicate ferromagnetic order to disappear. The non-stoichiometric, Mn-rich composition of the BMO nanoplate phase may also play a role in suppressing ferromagnetism, since to compensate for the extra charge, changes in bond density of the various Mn-O-Mn orbital configurations may occur which affect the Mn-O-Mn superexchange interactions.

BISMUTH IRON OXIDE NANOPARTICLES

In bulk form the multiferroic perovskite BFO has a high ferroelectric Curie temperature T_C = 1143 K and a high antiferromagnetic Néel temperature T_N = 643 K [28]. BFO is a G-type antiferromagnet with the Fe^{3+} magnetic moments coupled ferromagnetically within the (111) planes and antiferromagnetically between neighboring planes [29,30]. The presence of Fe^{3+} ions with a magnetic moment of $\mu_{Fe} = 3.70\ \mu_B$ was confirmed by neutron diffraction [31,32]. Neutron powder diffraction showed that the structure could be described using modulated magnetic ordering models such as a circular cycloid, an elliptical cycloid and a spin density wave [33]. A cycloidal spatially modulated spin structure is hence present in bulk samples, responsible for a cancellation of the macroscopic magnetization [34]. A helical spin structure with a long wavelength of 62 nm, incommensurate with the lattice spacing [35,36], results from the fact that the axis of spin alignment precesses through the crystal. As a result of the complex cycloidal spin structure easily being perturbed by strain, it has been suggested experimentally [37-40] and predicted theoretically [34], that in thin films weak ferromagnetism is present. In this work the focus lies on exploring the magnetic behavior of the BFO nanoparticles, since few results are available on nanoparticles, while size effects can lead to a modification of magnetic order as thin films indicate.

The BFO nanoparticles here were synthesized via the sol-gel method. Bismuth nitrate ($Bi(NO_3)_3 \cdot 5H_2O$) and iron nitrate ($Fe(NO_3)_3 \cdot 9H_2O$) in stoichiometric proportions (1:1 molar ratio) were dissolved in 2-methoxyethanol ($C_3H_8O_2$). The solution was adjusted to a pH value of 4–5 by adding 2-methoxyethanol and HNO_3. This mixture was stirred for 30 minutes at room temperature to obtain the sol, which was then kept at 80°C for 96 hours to form the dried gel powder. The dried powder was calcined in a temperature range of 400–600°C for 1 - 3 h in air. The optimal calcination temperature was 450 °C for 2 hours. The structure and morphology of BFO nanoparticles were investigated by powder XRD, and SEM. Magnetic measurements were obtained by variable-temperature SQUID magnetometry.

A SEM micrograph of the as-synthesized nanoparticle ensemble is depicted in Fig. 5, revealing a spherical morphology with average particle size of 20 nm. The XRD pattern of the as-synthesized material, depicted in Fig. 6, indicates a single-phase perovskite structure. The (111) peak splitting indicates a rhombohedral structure for the nanoparticle ensemble, consistent with the reported structure of BFO ceramics [41].

Figure 7 shows the H dependence of the magnetization M for the BFO nanoparticles at T= 10 K, 77 K and 298 K. The magnetic hysteresis shows ferromagnetism from 10 K to room temperature. As mentioned above, in bulk BFO single crystals the magnetization measurements are expected to exhibit antiferromagnetism [42,43]. Yet, weak ferromagnetism is often reported in polycrystalline BFO ceramics and thin films [44]. Spontaneous magnetization in as-synthesized BFO samples has been ascribed to cumulative effects of mixed Fe^{2+}/Fe^{3+} valence formation, of suppression of the helical spin structure, of an increase in canting angle, and/or of iron-rich nanoclusters [37,38,40,41,45-47]. A spin-glass behavior has also been observed in the $M(T)$ and $M(H)$ measurements for BFO films annealed in air atmosphere, further enhanced by

annealing the sample in an oxygen atmosphere and hence tentatively related to the formation of iron oxide nanoclusters or precipitates [40,47]. Yet in our samples no secondary phases are present according to the XRD and according to the EDS analysis contained in Table II. The BFO nanoparticle composition was found to be stoichiometric. Hence, we attribute the observed ferromagnetism to size effects resulting from the nanoparticle geometry influencing the cycloid spin structure. The wavelength of the fully developed incommensurate cycloid spin structure in bulk BFO is 62 nm [48], longer than the scale of our BFO nanoparticles. The cycloid spin structure characteristic of antiferromagnetism is interrupted by the particle surface in our BFO nanoparticles, an interruption that in thin films can induce ferromagnetic behavior [40,43].

Figure 8 contains the dependence on T of the magnetization M (T) under ZFC and FC conditions, with M (T) measured under applied H of 5000 Oe. At 5000 Oe the saturation magnetization is not reached, as can be observed in Fig. 7. Yet, the low-T value for the magnetization measured here, ~ 0.52 emu/g, compares well to the ~ 0.49 emu/g recently obtained for nanocrystalline films under FC conditions [49]. M (T) in Fig. 8 further shows irreversibility between FC and ZFC conditions over a wide range of T, a clear indication of spin-glass-like behavior (also observed in Ref. 49). For BFO, spin-glass-like behavior has been observed in both single-crystal and thin film samples (see *e.g.* Ref. 50). However, Fig. 8 contains evidence of spin-glass-like behavior in BFO nanoparticles. To provide context, the unique long-range spiral spin structure characteristic of bulk BFO will lead to spin-glass behavior differing from Ising systems. The spin-glass behavior may have long-range Coulumbic contributions to the electromagnons which are not pure spin waves [51]. Pinning of the incomplete spin spiral structure at the nanoparticle boundaries may also result in the experimental observation of spin-glass-like M (T). Further, spin-glass-like behavior in BFO has been ascribed to diffusion of domain walls, since the domain walls in BFO are known to influence both ferroelectric and ferromagnetic properties [52].

CONCLUSION

In both multiferroic materials $BiMnO_3$ and $BiFeO_3$, size effects modify the magnetic ordering, as demonstrated here by a synthesis of $BiMnO_3$ nanoplates and $BiFeO_3$ nanoparticles, followed by extensive compositional, structural and magnetic characterization. $BiMnO_3$ nanoscale plates were synthesized through co-precipitation. Magnetic measurements demonstrate a lack of magnetic ordering behavior which was explained on the basis of size effects and non-stoichiometry. $BiFeO_3$ nanoparticles were synthesized by a sol-gel method, and characterization shows the presence of $BiFeO_3$ at an average particle size of 20 nm (shorter than the cycloid length). Ferromagnetic properties and spin-glass-like behavior were observed in the $BiFeO_3$ nanoparticles. Spin-glass-like behavior can be ascribed to diffusion of domain walls, with possible contributions from pinning of the cycloid spin structure at the nanoparticle surface. Ferromagnetic behavior in the nanoparticles can be ascribed to an interruption or partial destruction of the long-wavelength cycloid spin structure characteristic of bulk $BiFeO_3$.

REFERENCES

[1] L. D. Landau and E. M. Lifshitz, *Electrodynamics of Continuous Media*, Pergamon Press, Oxford, 119 (1960).

[2] I. E. Dzyaloshinskii, Soviet Phys.- JETP **10**, 628 (1960).

[3] D. N. Astrov, Soviet Phys.- JETP **11**, 708 (1960).

[4] D. N. Astrov, Soviet Phys.- JETP **13**, 729 (1961).

[5] W. Prellier, M. P. Singh, and P. Murugavel, J. Phys. Condens. Matter **17**, R803 (2005).

[6] T. Zhao, A. Scholl, F. Zavaliche, K. Lee, M. Barry, A. Doran, M. P. Cruz, Y. H. Chu, C. Ederer, N. A. Spaldin, R. R. Das, D. M. Kim, S. H. Baek, C. B. Eom, and R. Ramesh, Nature Materials **5**, 823 (2006).

[7] N. A. Hill, J. Phys. Chem. B **104**, 6694 (2000).

[8] N. A. Hill, and A. Filippetti, J. Magn. Magn. Mater. **242**, 976 (2002).

[9] R. Ramesh, and N. A. Spalding, Nature Mater. **6**, 21 (2007).

[10] S. W. Cheong, and M. Mostovoy, Nature Mater. **6**, 13 (2007).

[11] G. A. Smolenskii, and V. A. Bokov, J. Appl. Phys. **35**, 915 (1964).

[12] W. Qu, X. Tan, R. W. McCallum, D. P. Cann, and E. Ustundag, J. Phys: Condens. Matter **18**, 8935 (2006).

[13] N. Hur, S. Park, P. A. Sharma, J. S. Ahn, S. Guha, and S. W. Cheong, Nature **429**, 392 (2004).

[14] G. Lawes, A. B. Harris, T. Kimura, N. Rogado, R. J. Cava, A. Aharony, O. Entin-Wohlman, T. Yildirim, M. Kenzelmann, C. Broholm, and A. P. Ramirez, Phys. Rev. Lett. **95**, 087205 (2005).

[15] Y. Yamasaki, S. Miyasaka, Y. Kaneko, J.-P. He, T. Arima, and Y. Tokura, Phys. Rev. Lett. **96**, 207204 (2006).

[16] K. Taniguchi, N. Abe, T. Takenobu, Y. Iwasa, and T. Arima, Phys. Rev. Lett. **97**, 097203 (2006).

[17] O. Heyer, N. Hollmann, I. Klassen, S. Jodlauk, L. Bohatý, P. Becker, J. A. Mydosh, T. Lorenz, and D. Khomskii, J. Phys.: Condens. Matter **18**, L471 (2006).

[18] M. Fiebig, J. Phys. D: Appl. Phys. **38**, R123 (2005).

[19] J. O. Cha, and J. S. Ahn, J. Korean Phys. Soc. **54**, 844 (2009).

[20] F. Gao, X. Y. Chen, K. B. Yin, S. Dong, Z. F. Ren, F. Yuan, T. Yu, Z. G. Zou, and J. M. Liu, Adv. Mater. **19**, 2889 (2007).

[21] Y. Yu Tomashpol'skii, E. V. Zubova, K. P. Burdina, and N. Yu. Venevtev, Sov. Phys. Crystallogr. **13,** 859 (1969).

[22] N. A. Hill, and K. M. Rabe, Phys. Rev. B **59**, 8759 (1999).

[23] F. Sugawara, S. Iida, Y. Syono, and S. Akimoto, Jpn. J. Phys. Soc. **20**, 1529 (1965).

[24] F. Sugawara, S. Iida, Y. Syono, and S. Akimoto, Jpn. J. Phys. Soc. **25**, 1553 (1968).

[25] T. Kimura, S. Kawamoto, I. Yamada, M. Azuma, M. Takano, and Y. Tokura, Phys. Rev. B **67**, 180401 (2003).

[26] A. M. Santos, A. K. Cheetham, T. Atou, Y. Syono, T. Yamaguchi, K. Ohoyama, H. Chiba, and C. N. R. Rao, Phys. Rev. B **66**, 064425 (2002).

[27] T. Atou, H. Chiba, K. Ohoyama, Y. Yamaguchi, and Y. Syono, J. Solid State Chem. **145**, 639 (1999).
[28] J. M. Moreau, C. Michel, R. Gerson *et al.* , J. Phys. Chem. Solids **32**, 1315 (1971).
[29] P. Fischer, M. Połomska, I. Sosnowska, and M. Szymański, J. Phys. C : Solid St. Phys. **13**, 1931 (1980).
[30] R. Przenioslo, A. Palewicz, M. Regulsk, I. Sosnowska, R. M. Ibberson, and K. S. Knight, J. Phys: Condens. Matter **18**, 2069 (2006).
[31] I. Sosnowska, R. Przenioslo, P. Fischer *et al.*, Acta Phys. Polonica A **86**, 629 (1994).
[32] I. Sosnowska, R. Przenioslo, P. Fischer, *et al.*, J. Magn. Magn. Mater. **160**, 384 (1996).
[33] R. Przenioslo, M. Regulski, and I. Sosnowska., Jpn. J. Phys. Soc. **75**(8), 084718 (2006).
[34] C. Ederer, and N. A. Spaldin, Phys. Rev. B. **71**, 060401 (2005).
[35] A. V. Zalessky, A. A. Frolov, A. K. Zvezdin *et al.*, J. Exp. Theor. Phys. **95**, 101 (2002).
[36] A. V. Zalessky, A. A. Frolov, T. A. Khimich *et al.* Europhys. Lett. **50**, 547 (2000).
[37] J. Wang, J. B. Neaton, H. Zheng, V. Nagarajan, S. B. Ogale, B. Liu, D. Viehland, V. Vaithyanathan, D. G. Schlom, U. V. Waghmare, N. A. Spaldin, K. M. Rabe, M. Wuttig, and R. Ramesh, Science **299**, 1719 (2003).
[38] H. Naganuma, and S. Okamura, J. Appl. Phys. **101,** 09M103 (2007).
[39] H. Bea, M. Bibes, S. Petit, J. Kreisel, and A. Barthelemy, Philos. Mag. Lett. **87** 165 (2007).
[40] P. K. Siwach, H. K. Singh, J. Singh, and O. N. Srivastava, Appl. Phys. Lett. **91**, 122503 (2007).
[41] S. T. Zhang, M. H. Lu, D. Wu, Y. F. Chen, and N. B. Ming, Appl. Phys. Lett. **87**, 262907 (2005).
[42] D. Lebeugle, D. Colson, A. Forget *et al.*, Phys Rev B **76**, 024116 (2007).
[43] F. M. Bai, J. L. Wang, M. Wuttig *et al.*, Appl. Phys. Lett. **86**, 032511 (2005).
[44] K. Takahashi, and M. Tonouchi, J Magn. Magn. Mater. **310**, 1174 (2007).
[45] J. B. Li, G. H. Rao, J. K. Liang *et al.*, Appl. Phys. Lett. **90**: 162513 (2007).
[46] W. Eerenstein, F. D. Morrison, J. Dho *et al.*, Science **307**, 1203a (2005).
[47] H. Béa, M. Bibes, S. Fusil *et al.*, Phys Rev B **74**, 020101 (2006).
[48] A. V. Zalesskii, A. K. Zvezdin, A. A. Frolov, and A. A. Bush, JETP Lett. **71**, 465. (2000).
[49] S. Vijayanand, M. B. Mahajan, H. S. Potdar, and P. A. Joy, Phys. Rev. B **80**, 064423 (2009).
[50] M. K. Singh, R. S. Katiyar, W. Prellier, and J. F. Scott, J. Phys.: Cond. Matter **21**, 042202 (2009).
[51] Yu. G. Chukalkin, and B. N. Goshchitskii, Phys. Status Solidi A **200**, R9 (2003).
[52] G. Catalan, H. Bea, S. Fusil, M. Bibes, P. Paruch, A. Barthelemy, and J. F. Scott, Phys. Rev. Lett. **100**, 027602 (2008).

FIGURES AND TABLES

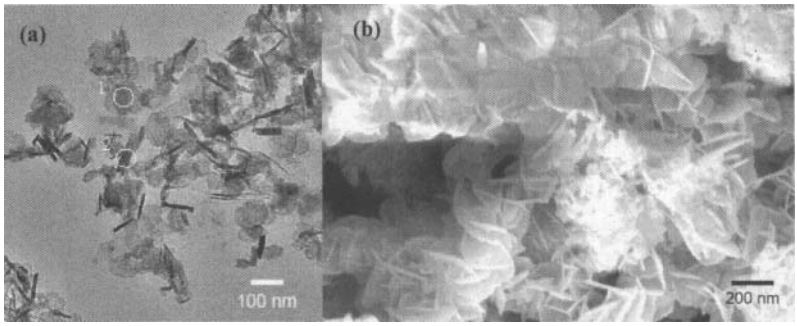

Figure 1. Micrographs of the BMO materials synthesis. (a): TEM and (b): SEM micrographs of the as-synthesized material, showing the $BiMnO_3$ nanoplates and the needle-like secondary phase.

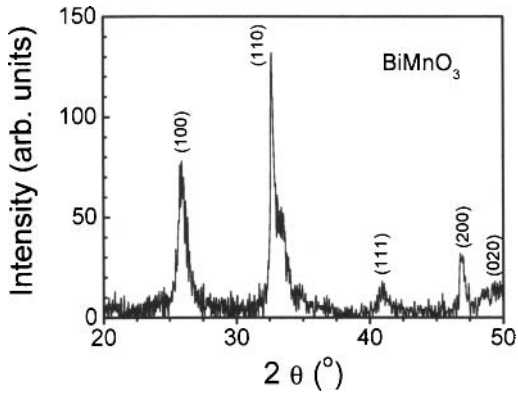

Figure 2. X-ray diffraction pattern (XRD) of the as-synthesized BMO material, showing a pattern dominated by the single-phase $BiMnO_3$ nanoplates.

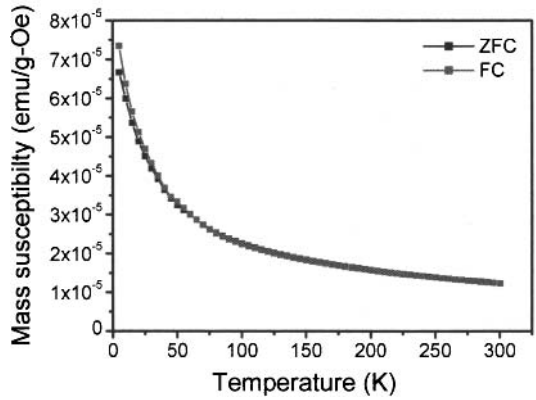

Figure 3. Temperature dependence of the mass susceptibility of the as-synthesized BMO material at an applied magnetic field of 5000 Oe. ZFC denotes zero-field cooled conditions, and FC denotes field-cooled conditions.

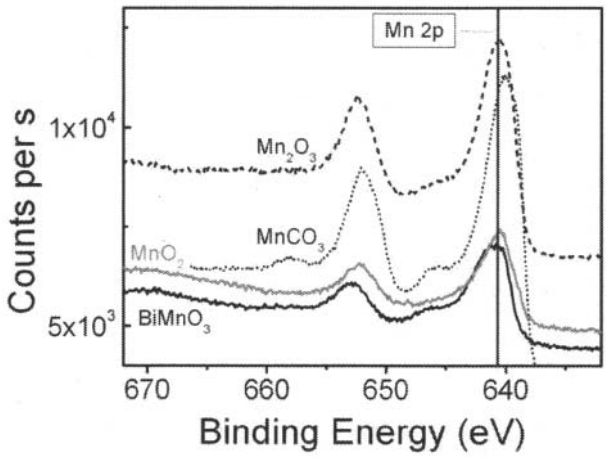

Figure 4. X-ray photoelectron spectroscopy (XPS) spectrum of the BMO nanoplates, and of standard samples of $MnCO_3$, Mn_2O_3 and MnO_2 used for comparison to identify the Mn valence.

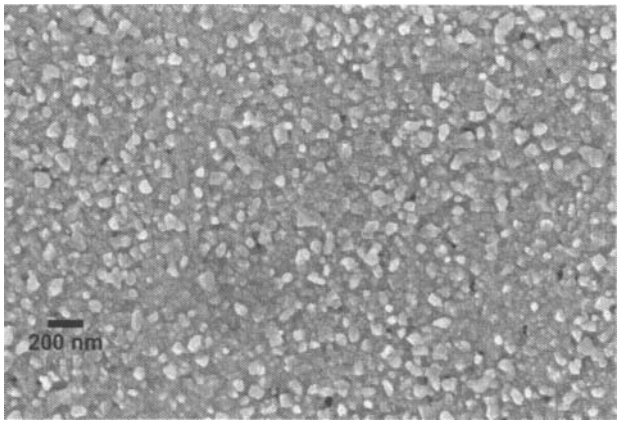

Figure 5. Scanning electron (SEM) micrograph of the as-synthesized BFO material, showing the $BiFeO_3$ nanoparticles.

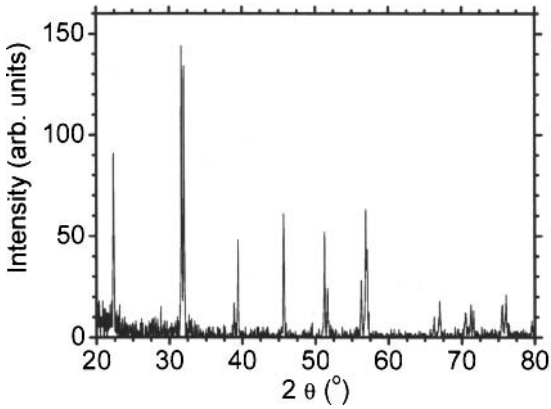

Figure 6. X-ray diffraction pattern (XRD) of the as-synthesized BFO material ($BiFeO_3$ nanoparticles), indicating a single-phase perovskite structure.

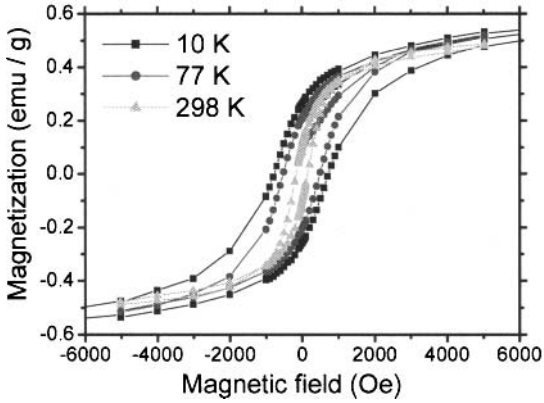

Figure 7. Magnetic field dependence of the magnetization (M) for the as-synthesized BFO material ($BiFeO_3$ nanoparticles) at T = 10 K, 77 K and 298 K. Ferromagnetic hysteresis is apparent from 10 K to room temperature.

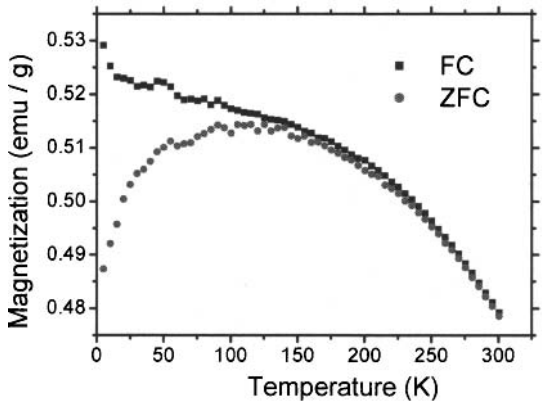

Figure 8. Temperature dependence of the magnetization (M) for the as-synthesized BFO material ($BiFeO_3$ nanoparticles) at an applied H = 5000 Oe (zero-field-cooled (ZFC) and field-cooled (FC) conditions).

Table I. (Top) EDS analysis of the needle-like phase in the as synthesized BMO matrix, conducted on the area marked as "2" in Fig. 1(a). (Bottom) EDS analysis of the nanoplate $BiMnO_3$ phase in the as-synthesized BMO matrix, conducted on the area marked as "1" in Fig. 1(a).

Element	Atomic %	Uncert. %	Correction	k-Factor
Mn(K)	5.83	0.43	0.99	1.451
Bi(L)	94.16	4.43	0.75	6.708

Element	Atomic %	Uncert. %	Correction	k-Factor
Mn(K)	58.28	2.97	0.99	1.451
Bi(L)	41.71	4.50	0.75	6.708

Table II. EDS analysis of the as-synthesized BFO matrix ($BiFeO_3$ nanoparticles).

Element	Atomic %	Uncert. %	Correction	k-Factor
Fe(K)	50.28	2.97	0.99	1.451
Bi(L)	49.71	4.50	0.75	6.708